

Chapter

Simulation Analysis of DFIG Integrated Wind Turbine Control System

Ramesh Kumar Behara and Kavita Behara

Abstract

Recently, scientists and academics are discovering progressive improvements in the arena of wind power technology economically and reliably, allowing them to produce electricity focusing on renewable energy resources. Wind turbines (WT) using the Doubly Fed Induction Generators (DFIGs) have attracted particular attention because of their advantages such as variable speed constant frequency (VSCF) operation, independent control capabilities for maximum power point tracking (MPPT), active and reactive power controls, and voltage control strategy at the point of common coupling (PCC). When such resources have to be integrated into the existing power system, the operation becomes more challenging, particularly in terms of stability, security, and reliability. A DFIG system with its control strategies is simulated on MATLAB software. This entails the rapid control prototype testing of grid-connected, variable speed DFIG wind turbines to investigate the WT's steady-state and dynamic behavior under normal and disturbed wind conditions. To augment the transient stability of DFIG, the simulation results for the active and reactive power of conventional controllers are compared with the adaptive tracking, self-tuned feed-forward PI controller model for optimum performance. Conclusive outcomes manifest the superior robustness of the feed-forward PI controller in terms of rising time, settling time, and overshoot value.

Keywords: renewable energy sources, DFIG's, MATLAB/SIMULINK, WT, MPPT, distribution network, wind energy

1. Introduction

The increasing demand for electrical power, and the rapid depletion and environmental concerns of fossil fuels have prompted the increased need for alternate forms of clean and sustainable energy sources. Globally there is an unassertive move away from unabated coal, and the rise of renewable energies from under 30% of generation in 2020 to above 40% in 2030 [1]. According to statistics (2021) put out by International Renewable Energy Agency (IRENA), an entire of 2,802,004 MW of electricity generation was produced worldwide in 2020, added by 53,824 MW of electricity generation from Africa [2]. The International Energy Agency (IEA) projected that the

worldwide energy mandate would be twofold by 2030 [3]. The global energy generation, ingesting, and financial development (1991–2017) swing displays a direct upsurge associated with the growing development of the global economy [4]. These cited worldwide trends of financial development mutually with industrial development and countryside electrification energy requirements are reflected in South Africa. South Africa's energy source is a mixture of 59% from carbon coal, 16% from petroleum, 3% from gasoline, 2% nuclear, and 20% from renewable resources and leftover [4, 5]. The worldwide cumulative swing of wind energy facility systems has speedily extended the wind energy facilities [6]. The wind is the gross effect of the pressure rise force, gravity, Coriolis, centrifugal and friction forces performing on the troposphere. The wind's aerodynamic features, lift and drag, angle of attack, and the effect of a high lift to drag ratio as the highest draft feature of the turbine rotor blade for effective wind power harvesting as explained in [7].

In [8], it was discussed how the twisted and tapered propeller-type rotor blades, could improve the angle of attack, rotor speed, and efficiency while reducing drag and bending stress. Betz equation evaluation of the wind energy conversion signifies that 59% optimum efficiency in which a conventional wind turbine can extract power from the wind [9]. Wind turbines generator systems are generally classified in lift and drag type, upwind and downwind type, and horizontal and vertical axis turbines. Most power utility networks operate either as $N + 1$ or $N + 2$ configuration criteria. $N-0$ configuration criterion is widely practiced in radial low voltage distribution networks [10]. A grid-connected wind energy system needs to meet certain standards before being integrated into the grid. Wind turbine generators control system (WTGCS) connects wind turbine generators to the grid, with a generation scheduling in place, that regulates the generator speed consequently adjusting the generator frequency, the voltage at the grid, active and reactive power flow using rotor side converter (RSC) and the grid side converter (GSC) and at the same time prefer to disconnect the wind turbines from the grid during faults, resulting in power losses, out of synchronization, and cascaded tripping of generation facilities [11].

The study in [12], clarifies in what way the controlled rotor current on the rotor side converter and a dynamic disruption elimination control by the resources of an extended state observer (ESO) controller the real and reactive stator powers produced by a wind power transformation method. In [13], an MPPT is combined with the DFIG stator flux oriented vector control to disassociate the control of real and reactive power produced by the DFIG centered wind turbine, with the generated power plattering as the dynamic energy reference for the DFIG. In [14], unit 3 directs the symmetrical and asymmetrical voltage rise and fall of the power grid-integrated DFIG, by including further current controller loops by disintegrating the vectorial references into progressive and undesirable signal indications. In [15], an open circuit stator negative sequence rotor current control system is applied, permitting the induced stator voltage to develop as unbalanced as the grid system voltage, henceforth allowing an even linking of DFIG to the power grid system. In [16], a wind speed assessment process centered on particle swarm optimization, and support vector regression, was evaluated to allow the MPPT control. The South African Renewable Energy Grid Code (SAREGC) published narration (2.9) in November 2016 stipulates the necessities for manufacturing standards, networking reliability, and unbalanced admittance to the power grid using RPPs.

This chapter aims to investigate the impact of wind energy penetration into the distribution grid for different percentages for the different scenarios of wind energy integration into the existing grid.

2. Aerodynamics, electrical, and drive train modeling

2.1 Aerodynamics modeling

The wind is the net result of the pressure gradient force, gravity, Coriolis, centrifugal and friction forces acting on the atmosphere. Since wind speed usually varies from one location to another and also fluctuates over time in a stochastic way, J.G. Slootweg [17] proposed a mathematical model that takes some landscape parameters to generate a wind speed $V_m(t)$ in (meter/sec) sequence for any location, as per equation one:

$$V_w(t) = V_{wa}(t) + V_{wr}(t) + V_{wg}(t) + V_{wt}(t) \quad (1)$$

Where, $V_{wa}(t)$ is a constant component, $V_{wr}(t)$ is a common ramp component, $V_{wg}(t)$ is a gust component, and $V_{wt}(t)$ is a turbulence component in (meter/sec).

The operation of a wind turbine can be characterized by its mechanical power output P_m through a cross-sectional area A normal to the wind as a function of wind speed V_w [18].

$$P_m = 0.5\rho AV_w^3 C_p(\alpha, \beta) \quad (2)$$

Where ρ is the air mass density, $A = \pi r^2$ is the turbine swept area, r is the turbine radius, and V_w is the wind speed. C_p is a nonlinear function of λ and β is referred to as the performance coefficient and is smaller than 0.59, given by [18, 19].

$$C_p = 0.5 \left[\frac{rC_f}{\lambda} - 0.022\beta - 2 \right] e^{-0.255\frac{rC_f}{\lambda}} \quad (3)$$

Where β is the turbine pitch angle, λ is the tip-speed ratio, and C_f is the blade design constant λ is defined by:

$$\lambda = \frac{r\omega_{tur}}{V_w} \quad (4)$$

Where ω_{tur} is the rotational angular speed of turbine blades in mechanical rad/sec.

$$P_{m \max} = \left(\frac{0.5\rho Ar^3 C_{p \max}}{\lambda_{opt}^3} \right) \omega_{tur}^3 = K_{opt} \omega_{tur}^3 \quad (5)$$

Eq. (5) indicates that P_{max} is proportional to the cube of turbine speed, hence the mechanical torque $T_{m \max}$ is:

$$T_{m \max} = K_{opt} \omega_{tur}^2 \quad (6)$$

2.2 Electrical modeling

A wounded-rotor induction motor can operate as a double-fed induction motor (DFIM) with the stator side windings openly attached to the three-phase power grid/load and the rotor side windings attached to a side-by-side moderately measured (20–30) % rating power converter as shown in **Figure 1**. As shown in **Figure 2**, an

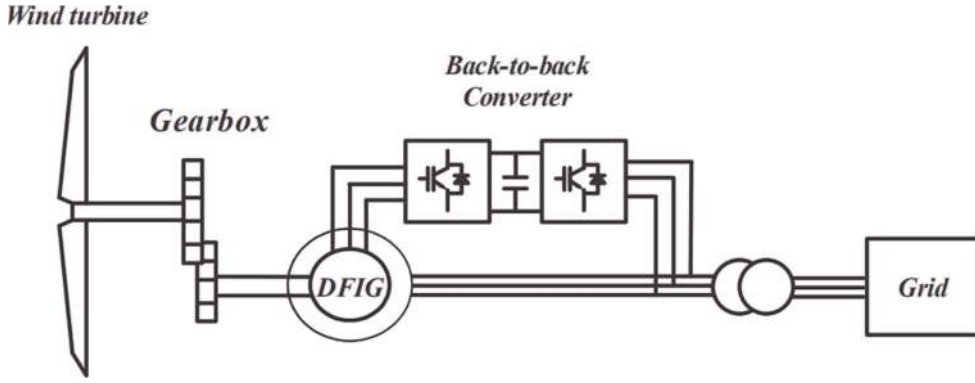


Figure 1.
Grid-connected DFIG [20].

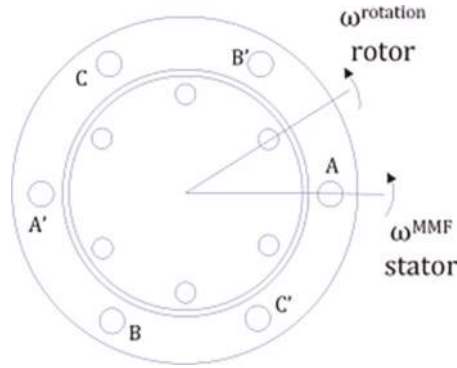


Figure 2.
Electrical modeling of an induction machine winding layout [21].

induction motor works on the interface principle between the stator and rotor magnetomotive forces (MMF). The stator side windings current produce an MMF revolving at power grid side frequency especially including an MMF in the rotor side windings. The rotor speed does not compliment the stator side MMF. This induced rotor MMF will rotate at the so-called slip frequency which possesses the subsequent value [21]:

$$\omega_{slip} = \omega_{mmf}^{rotor} = \omega_{mmf}^{stator} - \omega_{rotor} \quad (7)$$

Where, ω_{slip} is the slip frequency, corresponding to the frequency of rotor current and voltage, ω_{mmf}^{stator} is the stator or the grid frequency in (rad/sec), ω_{rotor} is the rotor rotating frequency (rad/sec). In both sub-synchronous and super-synchronous operations, the DFIM machine can be operated either as a motor ($0 < slip < 1$) with positive rotor torque or a generator ($slip < 0$) with negative rotor torque. The Park and Clark transform allowing the transformation of time-dependent variables into constant values. The per-unit electromagnetic torque equation expressed in d-q park reference is given by [22]:

$$T_e = \varphi_{ds} I_{qs} - \varphi_{qs} I_{ds} = \varphi_{qr} I_{dr} - \varphi_{dr} I_{qr} = L_m (I_{qs} I_{dr} - I_{ds} I_{qr}) \quad (8)$$

Neglecting the power losses associated with the stator and rotor resistances, the active and reactive stator powers for the DFIG are [22]:

$$P_s = \left(\frac{3}{2}\right) (V_{ds}I_{ds} + V_{qs}I_{qs}) \quad (9)$$

$$Q_s = \left(\frac{3}{2}\right) (V_{qs}I_{ds} - V_{ds}I_{qs}) \quad (10)$$

And the active and reactive rotor powers are given by:

$$P_r = \left(\frac{3}{2}\right) (V_{dr}I_{dr} + V_{qr}I_{qr}) \quad (11)$$

$$Q_r = \left(\frac{3}{2}\right) (V_{qr}I_{dr} - V_{dr}I_{qr}) \quad (12)$$

The overall system equations can also be re-written with relation to the rotating frames [21]:

$$P_T = P_s + P_r = \frac{3}{2} (V'_{qr}I'_{qr} + V'_{dr}I'_{dr} + V_{ds}I_{ds} + V_{qs}I_{qs}) \quad (13)$$

$$Q_T = Q_s + Q_r = \frac{3}{2} (V'_{qr}I'_{qr} - V'_{dr}I'_{dr} + V_{ds}I_{ds} - V_{qs}I_{qs}) \quad (14)$$

The torque expression and the stator reactive power, which are the control objectives of the rotor-side converter control, are shown in Eqs. 17 and 18. Where, p is the number of pole pairs of the generator, I_{qs} and I_{qr} are the q component of the stator and rotor current, I_{ds} and I_{dr} are the d component of the stator and rotor current, V_{qs} and V_{ds} are the q and d components of the stator voltage. The stator and rotor flux linkages in the synchronous reference frame are expressed as [23]:

$$\psi_s = L_s I_s + L_m I_r \quad (15)$$

$$\psi_r = L_m I_s + L_r I_r \quad (16)$$

The electromagnetic torque can be expressed using the $d - q$ components as following [23].

$$T_m = \frac{3}{2} p \frac{L_m}{L_s} (\psi_{qs} I_{dr} - \psi_{ds} I_{qr}) \quad (17)$$

$$Q_s = \frac{3}{2} (V_{qs} I_{ds} - V_{ds} I_{qs}) \quad (18)$$

2.3 Drive train model

Considering the mechanical aspect of the wind turbine, the mechanical representation of the drive train of the entire wind turbine is complex. Following four types of the drive train in wind turbine models are generally used [24].

1. Six mass drive train model.

2. Three mass drive train model.
3. Two mass drive train model.
4. one-mass drive train model.

Of the above four types of drive train models, the one that was modeled and implemented is the simplified form of the two mass-shaft model power train systems as shown in **Figure 3** consisting of a shaft and gearbox. As per the two-mass model of the drive train system described in [24], all masses are grouped into low and high-speed shafts. The inertia of the low-speed shaft comes mainly from the rotating blades and the inertia of the high-speed shaft. The input to the model for a two-mass system is established as torque T_A , which is gained by the aerodynamics methodology and the generator response torque T_e . The target is the deviations in the rotor speed ω_r and the generator speed ω_g . The deviations in the mechanically compelled torque T_m , the generator torque response T_e , and torque loss owing to friction T_{fric} , causes the variation of angular velocity ω_g^* [24].

$$T_m - T_e - T_{fric} = j_g \times \dot{\omega}_g \quad (19)$$

The change in the angular speed $\dot{\omega}_r$ is caused by the difference between the aerodynamic torque T_A and shaft torque T_s at a low speed shaft [24].

$$T_A - T_s = j_r \times \dot{\omega}_r \quad (20)$$

$$\dot{\omega}_g = \varphi_g'' \text{ and } \dot{\omega}_r = \varphi_r'' \quad (21)$$

T_m and T_s are connected by the gear ration, as $T_s = nT_m$

$$T_s = K_s \cdot \Delta\varphi + D_s \cdot \dot{\varphi} = K_s \cdot \Delta\varphi + D_s (\omega_r - \omega_g/n) \quad (22)$$

Where K_s is the stiffness constant and D_s is the damping constant of the shaft. Considering a two-mass free-swinging system the Eigen frequency is as follows:

$$\dot{\omega}_r = \frac{1}{J_r} \left(T_A - D_s \cdot \omega_r + \frac{D_s}{n} \dot{\omega}_g - K_s \int (\omega_r - \frac{\omega_g}{n}) dt \right) \quad (23)$$

$$\dot{\omega}_g = \frac{1}{J_g} \left(-T_e - \left(D_g + \frac{D_s}{n^2} \right) \omega_g + \frac{D_s}{n} \dot{\omega}_r - \frac{K_s}{n} \int (\omega_r - \frac{\omega_g}{n}) dt \right) \quad (24)$$

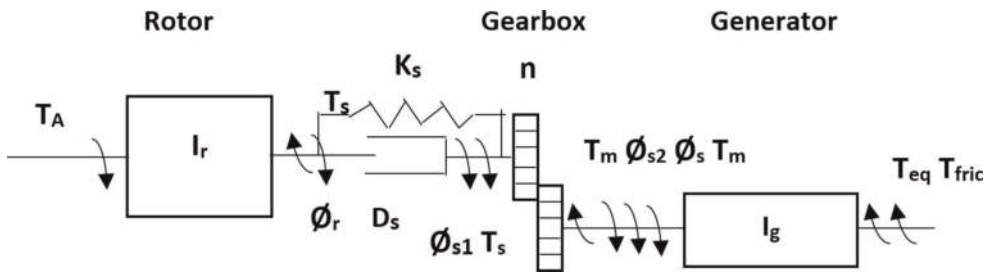


Figure 3. Schematic drawing of the two mass shaft drive train model [24].

Where, K_s is the stiffness constant and D_s is the damping constant of the shaft. Considering a two-mass free-swinging system, the Eigen frequency is given as:

$$\omega_{os} = 2\pi f_{os} = \sqrt{\frac{K_s}{J_{ges}}} \quad (25)$$

The total inertia of the free-swinging system on the low-speed is calculated by:

$$J_{ges} = \frac{J_r \cdot J_g \cdot n^2}{J_r + J_g \cdot n^2} \quad (26)$$

So, the stiffness constant K_s and the damping constant D_s of the low-speed shaft, with ξ_s as logarithmic decrement is:

$$K_s = J_{ges} \cdot (2\pi f_{os})^2 \quad (27)$$

$$D_s = 2\xi_s \cdot \sqrt{\frac{K_s J_{ges}}{\xi_s^2 + 4\pi^2}} \quad (28)$$

3. Control system

3.1 Conventional wind power control scheme

Owing to the alterations in the timing measures of the mechanical and electrical gestures, the DFIM-centered wind power control system has a multiple-layer control arrangement, with unified sub-systems. At the uppermost developed control stage, a maximum power point tracking procedure is applied to compute the generator speed set-point Ω_m^* to produce the DFIG target power set point T_{em}^* . The other control stage oversees the turbine pitch control scheme. The third and final control stage standardizes the generator torque, the real and reactive power, and the DC linkage voltage. The key limitations of the traditional control approach are explained in [25]. In the fractional load control process, the PI controller does not permit calibration of the commutation between the energy intensification and the momentary load depreciation, and at the full load control stage, the pitch-controlled generator speed directive can source acute power variations. Therefore, this study emphasizes the generator controller utilizing an adaptable tracing, self-adjustable PI controller framework. The suggested control system is disintegrated into various sub-categories entailing the fréchet derivative, the proportional, integral, and the derivative control. The PID control variables, K_p , K_i , and K_d are observed as the adaptable interfaces among the above sub-categories to self-adjusting these variables.

A reference current calculation and current control loop are presented as shown in **Figure 4** [26] and both the reference reactive power Q_{sref} and Q_{gref} are usually set to zero and can be modified depending on the grid requirements. The DC link reference voltage has a fixed value while the reference torque is determined by the maximum power point tracking control system. The vectorial control system of a grid-integrated DFIM is very similar to the traditional vectorial control system of a

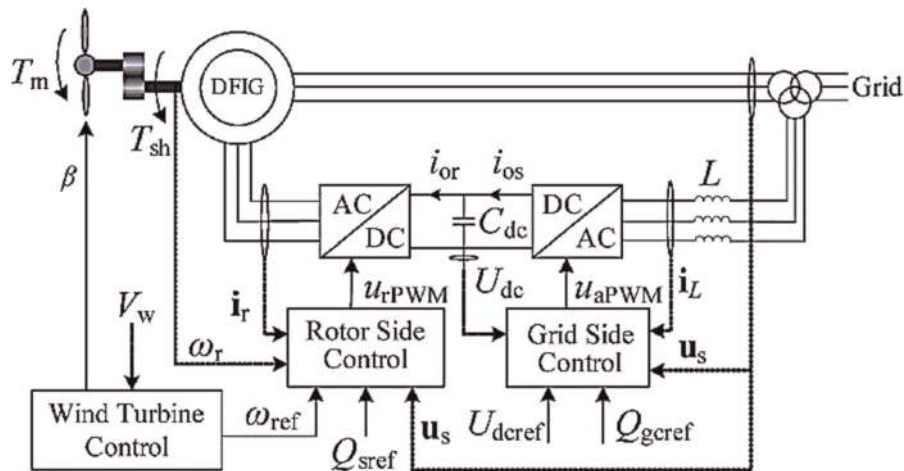


Figure 4. Reference values entered in DFIG back to back converter [26].

squirrel cage machine. DFIM is controlled in a synchronously revolving dq orientation structure, with the d axis adapted to the rotor flux space vector locus. The direct current is therefore related to the rotor side magnetic flux linkage although the quadrature current is related to the electromagnetic torque. By regulating autonomously, the two current modules, a disintegrated control between the torque and the rotor excitation current is achieved. Likewise, in the vectorial control system of a DFIM, the d and q axis components of the rotor current are controlled.

3.2 Maximum power point control

The most commonly used wind turbine control strategy is illustrated in **Figure 5**, and consists of four operation zones, this shows the wind speed as a function of the wind speed [27]. This resembles an operation at full load condition. Here, the

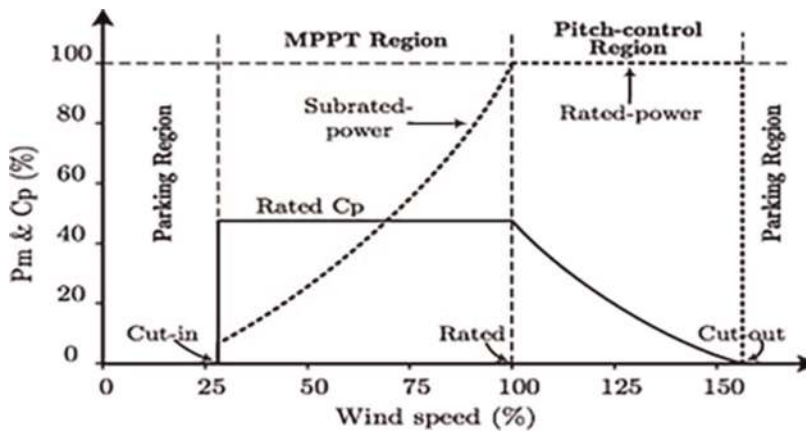


Figure 5. The operation zones for power point tracking for wind turbine [27].

mechanical power can be restricted moreover by changing the pitch or using torque control. Usually, the electromagnetic torque is retained at an insignificant value and regulates the pitch angle to retain the wind turbine at extreme speed to maintain power output at a higher than rated wind speed.

The maximum power deviation with the rotational speed of DFIM is pre-established for every individual wind turbine. Owing to the intermittent character of the wind, it is vital to comprise a control unit to be able to follow maximum peak irrespective of the wind speediness. Due to the adaptive tracking and self-tuning capabilities, the two best MPC control methods are described in [27] as indirect speed control and direct speed control. The direct speed controller (DSC) as shown in **Figure 6** follow the maximum power curve more narrowly with rapid dynamics. Observing the description of the tip speed ratio, the optimum VSWT rotating speed $\Omega_{t_{opt}}$ may be established from the wind speed V_w , whereas T_{em} is the turbine electromagnetic torque, Ω_m is rotating speed, $T_{t_{est}}$ is assessed turbine aerodynamics torque, and P_{max} is the maximum powering point.

$$\Omega_m^* = N \sqrt{\frac{T_{t_{est}}}{k_{opt_t}}} \quad (29)$$

$$P_{max} = \frac{1}{2} \rho \pi R^5 \frac{(C_{p_max})}{(\lambda_{opt}^3)} (\Omega_m^*)^3 \quad (30)$$

$$P_{MPPT} = K_{opt} (\Omega_m^*)^3 \quad (31)$$

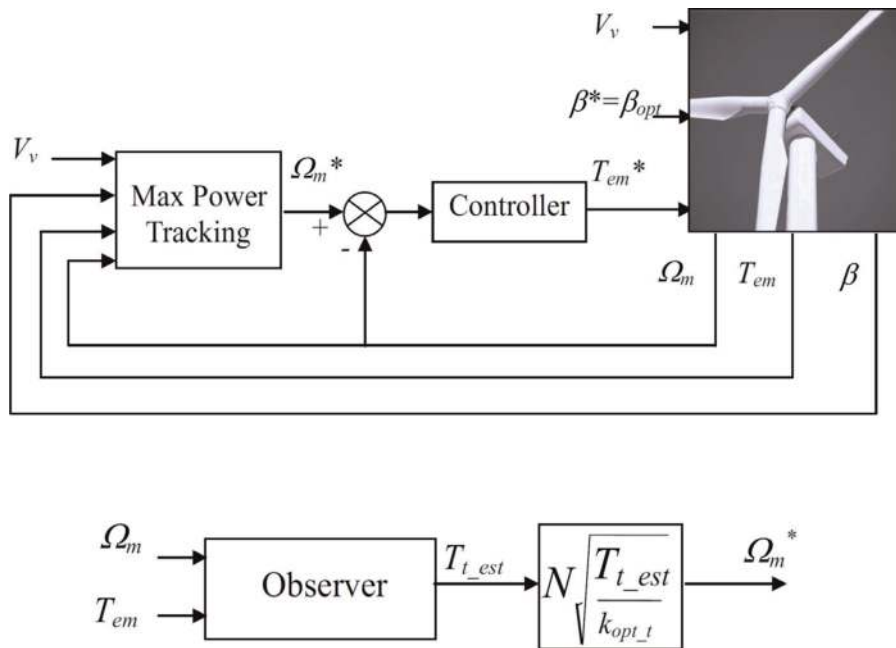


Figure 6.
 Direct speed control [27].

3.3 Rotor side control

The DFIG rotor variable's orientation must follow the orientation of the selected orientation parameter. Here, two algorithms are implemented, stator side voltage aligned control and stator side flux aligned control. Once this parameter vector is computed in the rotor side orientation structure, its comparative angle (δ) to the rotor side orientation structure is designed and the rotor parameters are altered into the novel control-reference structure, as shown in **Figure 7** [21].

Vector control is applied to the rotor side converter to control the stator's active and reactive power. The direct axis loop is used to control reactive power whereas the quadrature axis is for active power control. The rotor converter obtains evaluations of rotor circuit parameters and is accountable for handling the reactive power flow between the stator and the power grid as well as regulating the generator torque. Its input parameters are not associated with the stator orientation structure. Though, it is exactly the stator target that must be measured and controlled. For the RSC to calculate an output stable with the stator's parameters, the rotor parameters articulated in the rotor d-q orientation structure must be revolved to be oriented with the control orientation structure. The RSC controller MATLAB block diagram is shown in **Figure 8**.

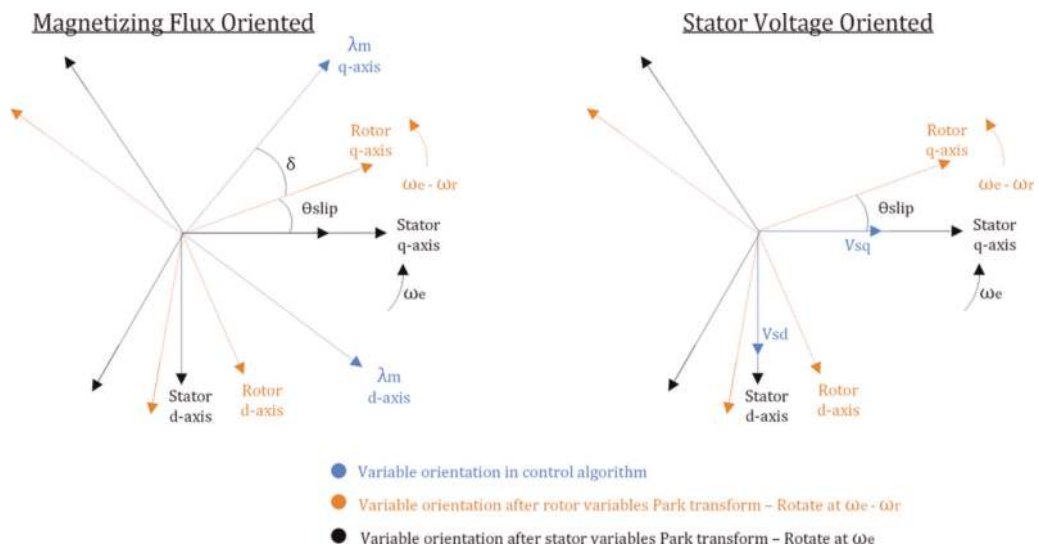


Figure 7. Reference frames used in park transform [21].

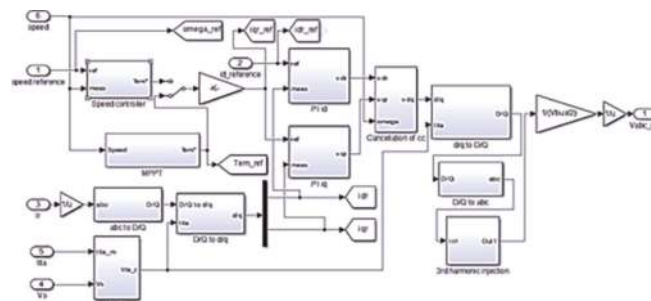


Figure 8. RSC controller MATLAB block diagram.

The equations used in the orientation process are [21]:

$$S_{r\ d} = S'_{r\ q} \sin(\delta) + S'_{r\ d} \cos(\delta) \quad (32)$$

$$S_{r\ q} = S'_{r\ q} \cos(\delta) - S'_{r\ d} \sin(\delta) \quad (33)$$

Where:

- S' represents a d-q rotor variable expressed in the rotor reference frame rotating at slip frequency.
- S represents the same rotor variable oriented along with the control reference frame.
- δ represents the alignment angle by which the rotor reference frame must be rotated.

3.4 Grid side control

The main objective of the grid side converter control model with ideal bidirectional switches as shown in **Figure 9** is to focus on the active and reactive powers delivered to the grid, keeping a constant DC-link voltage independent of the value and direction of the rotor power flow, and grid synchronization control. The grid side of the wind turbine system is composed of the grid side converter, the grid side filter, and the grid voltage. It converts voltage and currents from DC to AC, while the exchange of power can be in both directions from AC to DC (rectifier mode) and from DC to AC (inverter mode). The $d - q$ axis voltage V_{gd} and V_{gq} of the grid side converter from the original three phases V_{ga} , V_{gb} , V_{gc} is as below [27]:

$$V_{g\ d} = V_{g\ d} + R_g I_{g\ d} + L_g \frac{dI_{g\ d}}{dt} - \omega_s L_g I_{g\ q} \quad (34)$$

$$V_{g\ q} = V_{g\ q} + R_g I_{g\ q} + L_g \frac{dI_{g\ q}}{dt} + \omega_s L_g I_{g\ d} \quad (35)$$

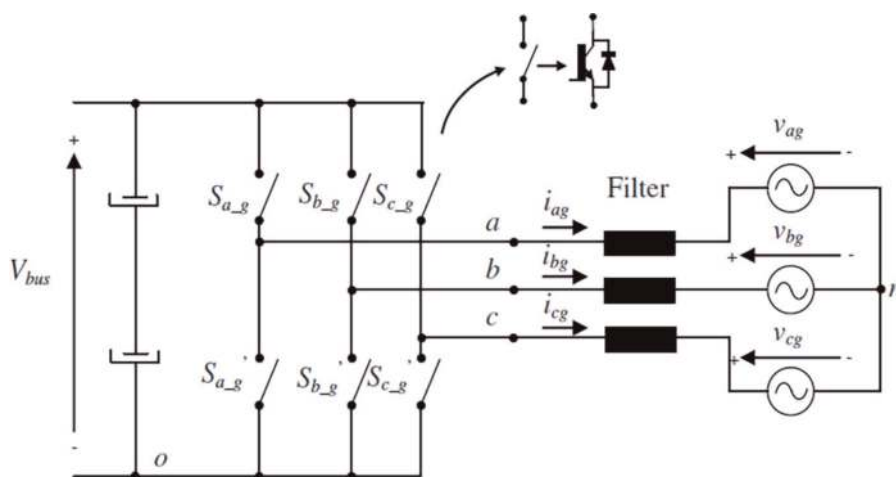


Figure 9. Simplified converter, filter, and grid model [27].

4. Simulation and discussion

4.1 Steady-state simulation

The system under study is shown in **Figure 10**. The 2 MW, 1500 rpm, 50 Hz, 690 V, 1760 A, and 12,732 Nm torque DFIG model was used to model and simulate the systems. The simulation was used to analyze the challenges with power system stability of integrating the WTG into the grid, considering intermittent wind characteristics and the problem of slip convergence. This task was executed by creating a steady-state Matlab function, to calculate the steady-state operation points and reveals how the rotor speed of the modeled DFIG involves the power flow of the studied system. Speed array and torque array were considered as inputs into the stimulated three-blade wind turbine connected with DFIG. Two different work frames of generation strategies $Q_s = 0$ and $I_{dr} = 0$ were considered here.

4.1.1 Steady-state simulation results and analysis

Simulations were carried out for variable wind speeds ranging from 5 m/s (cut-in speed) to 25 m/s (cut-off speed) in progressive steps of 2 m/s, with reactive power $Q_s = 0$, (red plot) and $I_{dr} = 0$ (green plot) as a control strategy separately. The results for the DFIG voltage, torque, generated real power, efficiency, and consumed reactive power in both the methods are plotted in **Figures 11–18**. The influence of two different generation strategies does not make big differences for variables such as T_{em} , P_t , P_s and P_r , however, some other variables such as I_s , I_r , Q_s , and Q_r , (**Figures 14–17**) was found to have some big differences in amplitudes, concerning rotor speed.

Figure 11 shows the DFIG's torque vs. speed characteristics, which stimulate the three-blade wind turbine with a minimum speed of 900 rpm and a maximum speed of 1800 rpm. The DFIG can perform above and under the synchronization speed for power generation. The generation model of DFIG matching negative torque values

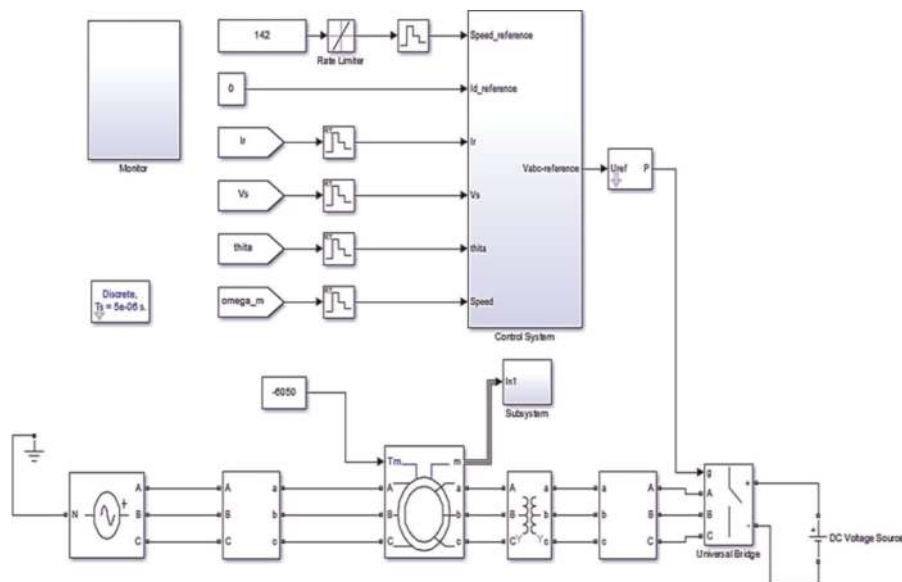


Figure 10.
Steady-state simulation program block model.

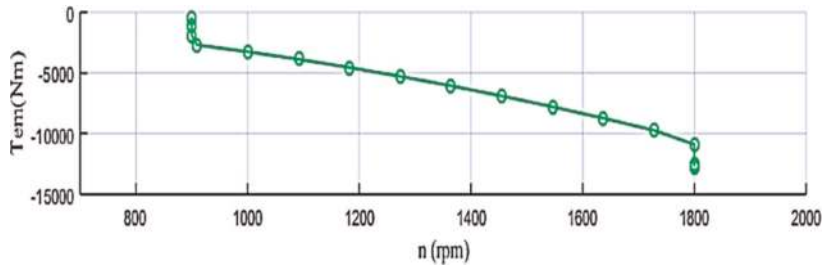


Figure 11.
 The graph of torque (T_{em}) vs. rotor speed (n).

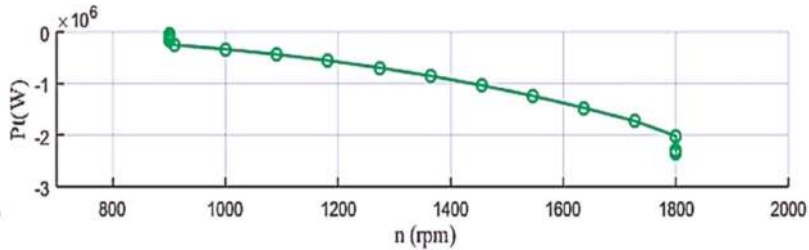


Figure 12.
 DFIG's active power P_t (W) vs. speed n (rpm).

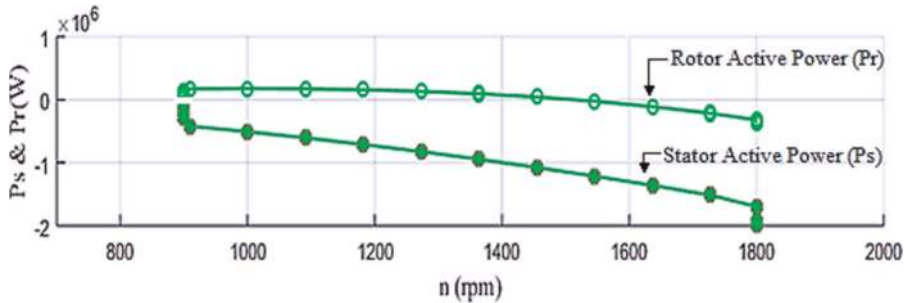


Figure 13.
 DFIG stator and rotor active power P_s & P_r (W) vs. speed n (rpm).

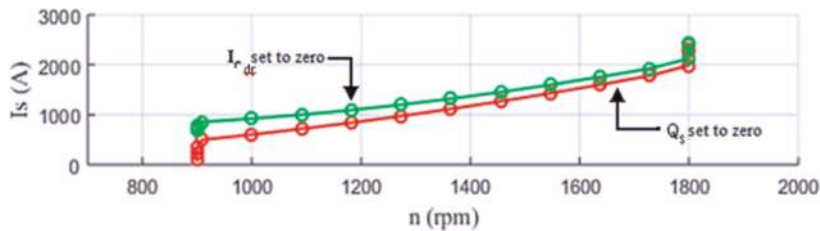


Figure 14.
 DFIG I_s (A) vs. n (rpm), red plot: $Q_s = 0$, green plot: $I_{dr} = 0$.

covers from the negative slip to the positive slip state. Therefore, the turbine target power and electromagnetic torque features of variable speed DFIGs are unlike the customized constant-speed induction machine. **Figure 12** shows the plotting for the total mechanical power of the turbine shaft, which is the product of torque and speed, from sub synchronous to super synchronous speed, with a maximum power value of

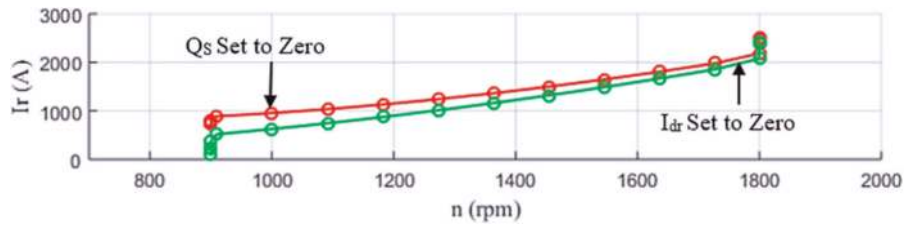


Figure 15.
DFIG I_r (A) vs. n (rpm), red plot: $Q_s = 0$, green plot: $I_{dr} = 0$.

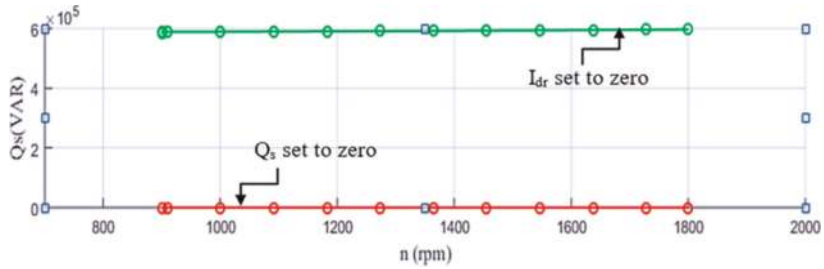


Figure 16.
DFIG Q_s (VAR) vs. n (rpm), red plot: $Q_s = 0$, green plot: $I_{dr} = 0$.

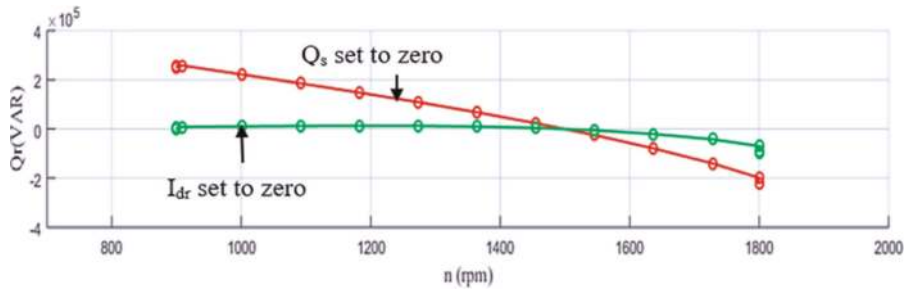


Figure 17.
DFIG Q_r (VAR) vs. n (rpm), red plot: $Q_s = 0$, green plot: $I_{dr} = 0$.

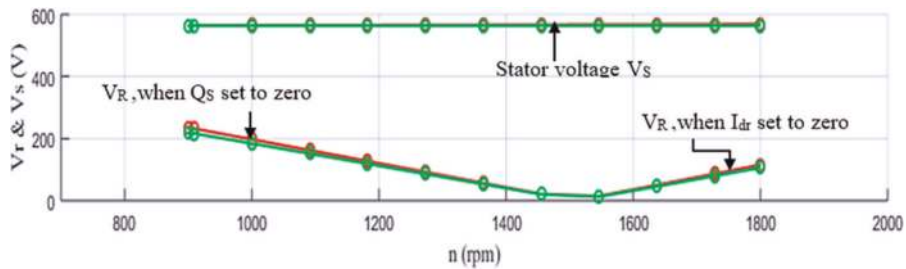


Figure 18.
DFIG V_r & V_s (V) vs. speed n (rpm), red plot: $Q_s = 0$, green plot: $I_{dr} = 0$.

–2.54 MW at 1800 rpm. **Figure 12** shows, the rotor’s active power P_r is absorbed by the induction machine at below synchronous speed, and the active power is supplied above the synchronous speed from the induction generator to the grid. **Figure 13**, shows, with $Q_s = 0$ (red plot) as an adopted control strategy the stator current value I_s is on the lower side. **Figures 14** and **15** shows during $I_{dr} = 0$ (green plot) as a control

Sn	Speed		Torque (N-m)		I _r		I _s		V _r	
	Steady-state	Simulation Model	Steady-state	Simulation Model	Steady-state	Simulation Model	Steady-state	Simulation Model	Steady State	Simulation Model
1	1182	1182	-4550	-4550	875	920	1090	1100	110	100
2	1356	1356	-6050	-6000	1160	1200	1325	1350	60	60
3	1691	1691	-9450	-9455	1770	1790	1850	1860	73	75

Table 1
 WT simulated parameters at defined DFIG speeds.

strategy the rotor current I_r is on the lower side and Q_s is on the higher side. **Figure 16** shows the rotor reactive power $Q_r = 0$ at synchronous speed 1500 rpm, with both control strategy $Q_s = 0$ and $I_{dr} = 0$, indicating the reactive power varies according to the wind turbine speed. **Figure 17** shows, a constant stator voltage V_s amplitude throughout the variable speed range, while the variable rotor voltage V_r amplitude is very low at synchronous speed 1500 rpm, with two peak voltage amplitudes at a minimum and maximum rotor speeds.

4.1.2 Evaluation of simulation modeling at defined speeds

Table 1 shows the specified wind turbine DFIG speeds that are compared and used to evaluate the simulation model parameters with the steady-state model parameters as obtained from **Figures 11–18**. The simulation graphs shown in **Figures 19** and **20** represent the torque vs. time and rotor current vs. time characteristics at 1356 rotor rpm and steady-state simulation period of 1.5 sec and 1691 rotor rpm at a steady-state simulation period of 2.0 sec for the entire modeling period of 3.0 sec. Simulated torque values -6050 Nm and -9450 Nm, rotor current values 1200 amps and 1790 amps, and stator current values 1325 amps and 1850 amps at pre-defined speeds are close to steady-state parameter values as shown in **Figures 11–18**.

4.1.3 Simulation model of DFIG using wind turbine MPPT block

In this section, a 2 MW stator power DFIG model and a three-blade wind turbine model with gear ratio $n = 100$, blade radius 42 m, $C_p = 0.42$, and $\lambda_{opt} = 7.2$ were used for the wind turbine maximum power point tracking simulation control as shown in **Figure 21**. **Figures 22** and **23** show the wind turbine MPPT simulation model characteristics at 8 m/sec and 10 m/sec of wind speed. Observed in **Figure 11**, the torque response for the wind speed and i_q current indicates that more oscillations occur at the low torque due to the fact reduced mechanical inertia. The more the mechanical inertia, the more the torque oscillations. On achieving the steady-state condition at

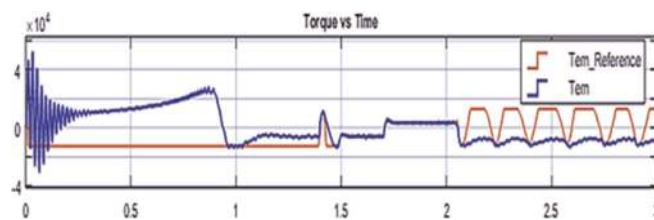


Figure 19.
Torque vs. time graph @ 1356 rotor rpm and @ 1691 rotor rpm.

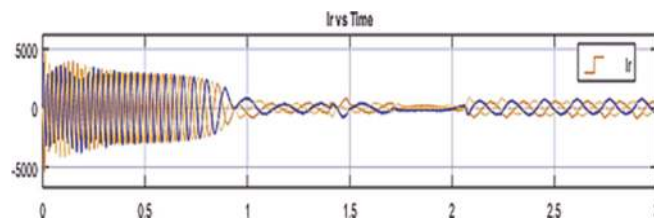


Figure 20.
 I_r vs. time graph @ 1356 rotor rpm and @ 1691 rotor rpm.

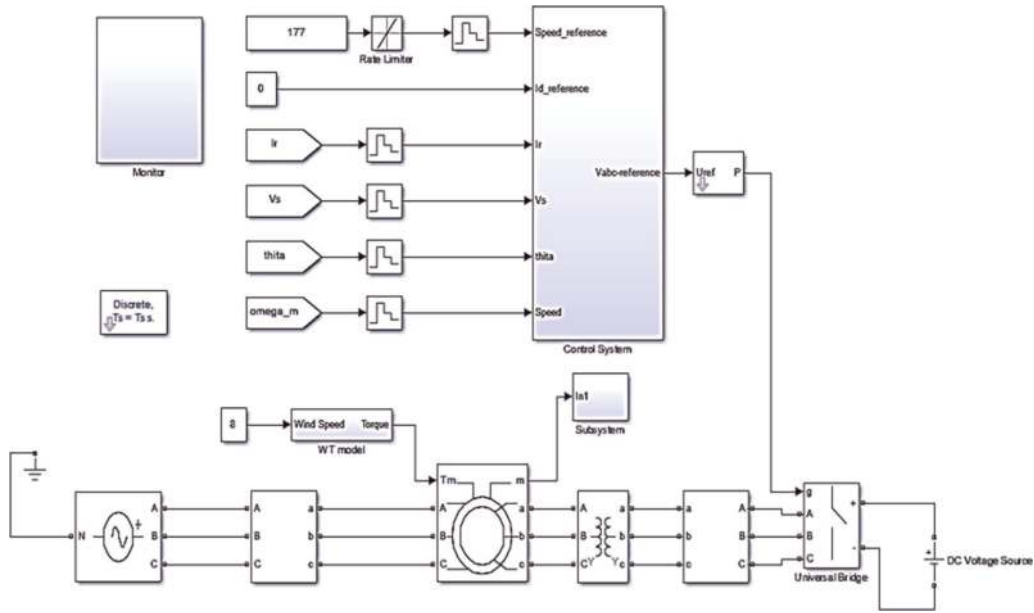


Figure 21.
 WT MPPT control model.

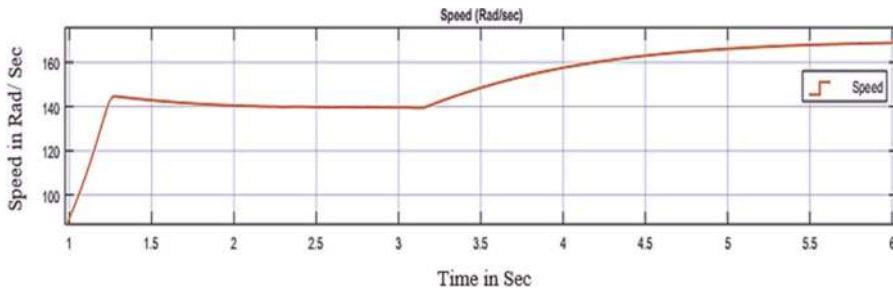


Figure 22.
 The dynamic state WT MPPT graph of speed vs. time (sec).

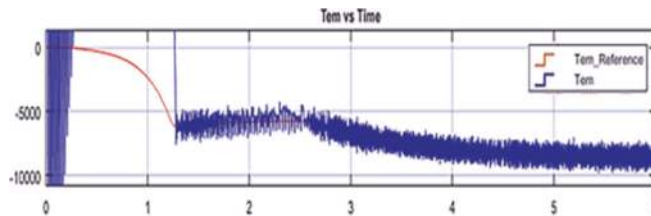


Figure 23.
 WT MPPT torque vs. time characteristic curve.

2 sec of modeling time, wind turbine speed and correspondence torque values were tabled for angular speed of 140 rad/sec, at a torque of -5500 Nm, and a mechanical wind turbine power output approximately equal to 770 kW was obtained. Further, the wind speed was increased from 8 m/sec to 10 m/sec and the steady-state simulation at 6 sec of modeling time was observed. On achieving the steady-state at 6 sec of modeling time, wind turbine speed and correspondence torque values were tabulated for 170 rad/sec, at -8800 Nm respectively and a mathematical wind turbine power

outcome equivalent to 1.49 MW was recorded. These two simulated outcomes are very close to the steady-state characteristics graph numerical values as shown in **Figures 11** and **12**.

5. Conclusions

This study was to focus on investigating the influences of the integration of wind power generators into the power grid systems. The rotor side converter control unit is utilized for, real and reactive power control by regulating the rotor current and the speed of the DFIG. With the computed stator voltage, stator current, rotor current, and the rotor location by encoder response signal the active PI measured and controlled procedure results in a considerable enhancement in control system sturdiness and advances its indemnity to produced system noise. The engaged PI control unit attests to the grid side converter control by sustaining the stable generated power frequency and voltage with the grid frequency and voltage. The controller scheme and the simulation mode controller employed for the study assure the wind generator supplying into the grid at varying wind speeds behaves like a synchronous generator, at a zero Hz rotor frequency.

Acknowledgements

I wish to thank the almighty God for giving me life and enabling me to reach the heights that I have reached.

I wish to thank my parents and my siblings, for their tireless and relentless love, continuous support, and the countless sacrifices they have made on my behalf. To my family, for being great inspirations and believing in us even when we have stopped believing in ourselves. This would not have been possible without the family's help.

Finally, I wish to everyone not mentioned above but directly or indirectly contributed to our work, your input is much acknowledged.

Abbreviations

DFIGs	Double Fed Induction Generators
DSC	Direct Speed Control
ESO	Extended State Observer
GSC	Grid Side Converter
IEA	International Energy Agency
IRENA	International Renewable Energy Agency
MMF	Magnetomotive Force
MPPT	Maximum Power Point Tracking
PCC	Point of Common Coupling
RSC	Rotor Side Converter
SARGEC	The South African Renewable Energy Grid Code
VSCF	Variable Sped Constant Frequency
WECS	wind energy control System
WT	Wind Turbines
WTGCS	Wind turbine generators control system

C_f	Turbine blade density constant
C_p	Coefficient of performance
E	Kinetic energy of air mass of m kg
K_s	Stiffness constant
D_s	Damping constant
P_s	Stator active power in watts
P_r	Rotor active power in watts
Q_s	Stator reactive power in watts
Q_r	Rotor reactive power in watts
R	Turbine blade radius in meters
T_e	Per-unit electromagnetic torque in d-q park reference newton/meter
T_f	Turbine friction torque in newton/meter
T_{mmax}	Turbine maximum torque in Newton/meter
$V_m(t)$	Wind Speed in meter/sec
$V_w(t)$	Wind Speed of air mass of m Kg in meter/sec
$V_{wt}(t)$	Wind Speed turbulence component speed in meter/sec
$V_{wa}(t)$	Wind Speed constant component speed in meter/sec
$V_{gt}(t)$	Wind Speed gust component in meter/sec
ρ	Air density in Kg/m ³
β	Turbine blade pitch angle
λ	Turbine blade tip speed ratio
ω_{tur}	Turbine rotational angular speed in mechanical radian/sec
ω_{slip}	Slip frequency
ω_{mmf}^{stator}	Slip frequency corresponding to the frequency of rotor current and voltage in radian/sec
ω_{rotor}	Rotor rotating frequency in radian/sec
ω_r	Rotor speed in radian/sec
ω_g	Generator speed in radian/sec
Ψ_s	Stator flux linkage in synchronous frame weber
Ψ_r	Rotor flux linkage in synchronous frame weber

Author details

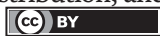
Ramesh Kumar Behara^{1*} and Kavita Behara²

1 University of KwaZulu Natal, Durban, Republic of South Africa

2 Mangosuthu University of Technology, Durban, Republic of South Africa

*Address all correspondence to: bramesh250770@gmail.com

IntechOpen

© 2022 The Author(s). Licensee IntechOpen. This chapter is distributed under the terms of the Creative Commons Attribution License (<http://creativecommons.org/licenses/by/3.0>), which permits unrestricted use, distribution, and reproduction in any medium, provided the original work is properly cited. 

References

- [1] India Energy Outlook. India Energy Outlook 2021 – Analysis - IEA. India Energy Outlook, 2021
- [2] Renewable I and Agency E. Renewable Energy Statistics 2021. 2021
- [3] European Wind Energy Association and Greenpeace. WIND FORCE 12 a blueprint to achieve 12% of the world's electricity from wind power by 2020. Wind Force. 2005;12(June 2005):1-52
- [4] Dr P, Li M. World energy 2017-2050: Annual report. World Energy Reports. 2017;(June):1-29
- [5] Scholtz L, Muluadzi K, Kritzinger K, Mabaso M & Forder S. Renewable Energy: Facts and Futures - The energy future we want. 2017
- [6] Abdelhafez AA, Alruways SH, Alsaif YA, Althobaiti MF, AlOtaibi AB & Alotaibi NA. Reactive Power Problem and Solutions: An Overview. Journal of Power and Energy Engineering. 2017;5(5):40–54
- [7] Robert LMT, Gabler E, Petersen JF. Atmospheric pressure, winds, and circulation patterns. Weather. 2008: 113-137
- [8] Wang T. A brief review on wind turbine aerodynamics. Theoretical and Applied Mechanics Letters. 2012;2(6):1-8
- [9] Ragheb M, Ragheb AM. Wind turbines theory - the Betz equation and optimal rotor tip speed ratio. Intechopen. 2011;1(1):1-22
- [10] Mcdonald JD, Wojszczyk B, Flynn B, Voloh I. Distribution systems, substations, and integration of distributed generation. In: Encyclopedia of Sustainability Science and Technology. Springer Science+Business Media New York; 2013. pp. 1-63
- [11] Sewchurran S, Davidson IE. Introduction to the south African renewable energy grid code version 2.9 requirements (part III - discussions and conclusions). IEEE AFRICON: Science, Technology and Innovation for Africa. 2017;17(4):1231-1235
- [12] Jabal Laafou A, Ait Madi A, Addaim A, Intidam A. Dynamic modeling and improved control of a grid-connected DFIG used in wind energy conversion systems. Mathematical Problems in Engineering. 2020;2020(10):1-15
- [13] Monteiro CP and Da Costa JS. Simulation and Control of a Dfig-based Wind Turbine. Res. gate NECEC. 2020. no. December, p. 9
- [14] Boukili Y, Aguiar AP, Carvalho A. A DFIG-based wind turbine operation under balanced and unbalanced grid voltage conditions. IFAC-PapersOnLine. 2020;53(2):12835-12840
- [15] Akrama K, Xiao Ming H, Mohamed AK, and Paul B. Doubly Fed Induction Generator Open Stator Synchronized Control during Unbalanced Grid Voltage Condition. 2020;13(3155):1-13
- [16] Eltamaly AM, Al-Saud M, Sayed K, Abo-Khalil AG. Sensorless active and reactive control for DFIG wind turbines using opposition-based learning technique. Sustain. 2020;12(9): 1-14
- [17] Slootweg JG, Polinder H, Kling W. Dynamic modelling of a wind turbine with doubly fed induction generator. IEEE Power Engineering Society

Transmission and Distribution
Conference. 2001;**01**(9):644-649

[18] Singh M. Dynamic Models for Wind
Turbines and Wind Power Plants. 2011

[19] Zhang Y, Zhang L, Liu Y.
Implementation of maximum power
point tracking based on variable speed
forecasting for wind. PRO. 2019;**158**(7):
1-18

[20] Abo-Khalil AG. Modeling and
Control Aspects of Wind Power Systems.
Impacts of wind farms on power system
stability. Wind Power In Power System.
2013:133-151

[21] Jonathan Fournier. Modeling,
Control and Experimental Validation of
a DFIG-based wind Turbine test bench.
Universitat Politecnica de Catalunya,
Barcelona, Catalonia Institute for Energy
Research (IREC). 2013

[22] Badreldien M, Usama R, El-wakeel A,
Abdelaziz AY. Modeling, Analysis, and
Control of Doubly Fed Induction
Generators for Wind Turbines.
ICEENG Conference ICEENG-9. 2014:1-18

[23] Arnaltes S, Rodriguez-Amenedo JL,
Montilla-D Jesus ME. Control of variable
speed wind turbines with doubly fed
asynchronous generators for stand-alone
applications. Energies. 2018;**26**(11):1-16

[24] Soriano LA, Yu W, Rubio JDJ.
Modeling and control of wind turbine.
Mathematical Problems in Engineering.
2013;**2013**:1-13

[25] Prabakar K. Gain Tuning of
Proportional-Integral Controller Based
on Multiobjective Optimization and
Controller Hardware-in-loop Microgrid
set up. 2015

[26] Michalke G, Hansen AD,
Hartkopf T. Control strategy of a

variable speed wind turbine with
multipole permanent magnet
synchronous generator. European Wind
Energy Conference and Exhibition.
2007:1371-1378

[27] Abad G, Lopez J, Rodriguez M,
Marroyo L, Iwanski G. Doubly Fed
Induction Machine. 2011th ed. Hoboken,
New Jersey, Wiley Publication: John
Wiley & Sons, Inc.; 2011